# Optimal Common-Mode Voltage for Grid-Tied Photovoltaic Cascaded H-Bridge Inverters Under Severe Power Imbalances

Rivera, Felipe Calderon; Angulo, Alejandro; Acuna, Pablo; Mora, Andres

**DOI**
10.1109/TIE.2023.3337545

**Publication date**
2023

**Document Version**
Final published version

**Published in**
IEEE Transactions on Industrial Electronics

# Optimal Common-Mode Voltage for Grid-Tied Photovoltaic Cascaded H-Bridge Inverters Under Severe Power Imbalances

Felipe Calderón Rivera, *Student Member, IEEE*, Alejandro Angulo, *Member, IEEE*, Pablo Acuna, *Member, IEEE*, and Andrés Mora, *Member, IEEE*

***Abstract*—This article deals with the control problem of injecting balanced grid currents from a grid-tied photovoltaic cascaded H-bridge (CHB) inverter under severe interphase power imbalances. Existing solutions are hindered by the additional harmonic content required at the inverter output voltages. Therefore, a mathematical formulation for which the solution has minimal harmonic content is proposed. The proposed solution, optimal common-mode voltage (OCMV), has an analytical form that allows deducing and analyzing the CHB operating area. The real-time implementation of the OCMV requires solving a nonlinear two-variables system; thus, an iterative and distributed algorithm is designed. By doing so, the proposed OCMV can be fully formulated and implemented using a real-time control platform. The experimental validation was carried out in a scale-down 3 kW grid-tied seven-level CHB inverter governed by phase-shifted model predictive control. The laboratory results show that the proposed OCMV allows obtaining symmetrical grid currents while maintaining low-distorted inverter output voltages.**

***Index Terms*—Cascaded H-bridge (CHB) inverter, interphase power imbalance, optimal control, phase-shifted model predictive control (PS-MPC), zero-sequence voltage (ZSV).**

## I. Introduction

SOLAR photovoltaic (PV) installations have increased despite the worldwide economic contractions caused by the Covid-19 lockdowns. In current markets, solar PV is among the most affordable new electricity technologies [1]. Hence, in 2021, the economic competitiveness and the attractiveness of power purchase agreements elucidated the global capacity additions of large-scale PV (LSPV) plants increased by approximately 20%, with 100 GW of new installations, encouraging the energy matrix decarbonization [2].

The LSPV plants often comprise tens to hundreds of power stations, each rated at more than 100 kW. The energy generated by each station is clustered in the main substation and transmitted to the power system [3]. In particular, a power station traditionally includes an MV transformer, a line filter, and a centralized two-level inverter fed by a PV array with hundreds of PV modules in series and parallel connections [4], [5]. This layout has at least three drawbacks. First, the low voltage at the inverter output terminals makes it necessary to use a high-cost and high-size MV transformer to reduce losses in transmitting the energy to the main substation [5], [6]. Second, due to the high-distorted voltages produced by the two-level inverter, the strict grid-code compliance obligates using *LCL* filters [7]. Third, the granularity of the maximum power point tracking (MPPT) is minimal because the available power from a power station depends on the unique MPPT strategy carried out by its central inverter [4], [5], [6].

Accordingly, the cascaded H-bridge (CHB) inverter has been proposed to enhance the overall LSPV plant layout by reducing the number of MV transformers [8]. Higher voltage and power levels with low-distorted inverter voltages are obtained due to the cascaded connection of submodules (SMs), reducing the filtering requirements. Moreover, its modular structure increments the MPPT's granularity [5], [6]. However, the well-known interphase power imbalance problem arises when independent PV arrays are connected to each CHB's SM [5], [9]. Instead of focusing on the current controller to attain balanced grid currents from an unbalanced power source, this issue requires the injection of a zero-sequence voltage (ZSV) at the modulating signals, i.e., a common-mode voltage at the inverter phase output terminals [8], [10], [11], [12], [13], [14]. Adopting a ZSV injection method depends on two main factors: the interphase power imbalance level and the available dc voltage in SMs. A pure-sinusoidal ZSV is sufficient to deal with light power imbalances; thus, H-bridges (HBs) operate in the linear range. However, if the ZSV injection implies the HBs saturation, a ZSV

Manuscript received 23 July 2023; revised 16 October 2023; accepted 13 November 2023. Date of publication 15 December 2023; date of current version 5 June 2024. This work was supported in part by the ANID under Grant Fondecyt Regular 1210625, Grant 1231265, and Grant 1231030; in part by the FB0008–Advanced Center for Electrical and Electronics Engineering; and in part by the Fondequip under Grant QM210117. *(Corresponding author: Felipe Calderón Rivera.)*

Felipe Calderón Rivera is with the Department of Electrical Sustainable Energy, Delft University of Technology, 2628 CD Delft, The Netherlands (e-mail: F.A.CalderonRivera@tudelft.nl).

Alejandro Angulo and Andrés Mora are with the Department of Electrical Engineering, Universidad Técnica Federico Santa María, Valparaíso 2390123, Chile (e-mail: alejandro.angulo@usm.cl; andres.mora@usm.cl).

Pablo Acuna is with the Department of Electrical Engineering, Universidad de Talca, Curicó 3340000, Chile (e-mail: pablo.acuna@ieee.org).

Color versions of one or more figures in this article are available at https://doi.org/10.1109/TIE.2023.3337545.

Digital Object Identifier 10.1109/TIE.2023.3337545

with harmonics is needed to maintain the current symmetry and control.

For this problem, Yu et al. [10] proposed the fundamental-frequency zero-sequence injection, which injects a pure-sinusoidal ZSV. On the other side, the double $1/6$ third harmonic injection, the reduced third harmonic injection, and the double min–max zero-sequence injection include harmonics to extend the interphase power imbalance range. Subsequently, in [11], the optimal zero-sequence injection (OZSI) permits utilizing all the available dc voltage by injecting an additional harmonic content that makes the phase voltage peak as low as possible. Injecting this high-distorted ZSV maximizes the interphase power imbalance compensation range; however, the harmonic content drastically increases no matter the asymmetry level of the available interphase power. Later, Sochor and Akagi [12] proposed a simpler ZSV consisting of a rectangle waveform and a third-harmonic component obtaining a smaller power imbalance range with similar harmonic distortion than the OZSI. Thereupon, Sharma and Das [13] enhanced the pure-sinusoidal ZSV injection, including reactive power exchange with the grid, and Aguilera et al. [8] allowed the instantaneous calculation of the fundamental ZSV according to the interphase power imbalances.

Given this background, this article presents a novel mathematical formulation for the grid-tied CHB inverter interphase power imbalance problem. The model is based on optimization and is written as a continuous time domain problem, where arbitrary power factors and instantaneous variable values are considered. The optimal solution, optimal common-mode voltage (OCMV), allows balanced grid currents to be injected under severe power imbalance conditions, guaranteeing minimum harmonic distortion in all feasible operation zone. For the OCMV, analytical and numerical solutions are identified, both implementable in real time, and a detailed analysis of the admissible imbalance levels that this solution allows is carried out. The main contributions declared by the authors are threefold.

1) A novel mathematical formulation for the grid-tied inverters' interphase power imbalance problem is proposed, whose optimal solution, the OCMV, has minimal harmonic content.
2) The OCMV analytical form and its feasible domain are derived, identifying the benefits of our approach concerning state-of-the-art ZSV injection methods.
3) A distributed and iterative numerical method to calculate the OCMV in real time is proposed, and its performance utilizing a scale-down seven-level CHB converter using a phase-shifted model predictive control (PS-MPC) scheme is evaluated experimentally.

The rest of this article is organized as follows. Section II presents a mathematical formulation for the grid-tied CHB inverter interphase power imbalance problem. In Section III, we get a formula for the OCMV, analyze its feasible domain, and propose a distributed algorithm for calculating the OCMV in real time. Then, a numerical analysis of our approach is made in Section IV. Experimental evaluation using a scale-down 3 kW seven-level CHB converter is accomplished in Section V. Finally, Section VI concludes this article.

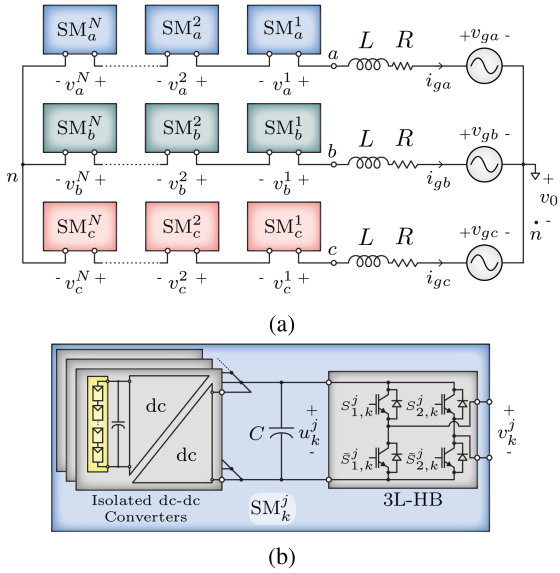


Fig. 1. Grid-tied PV CHB inverter. (a) Circuit diagram. (b) Two-stage SM configuration.

## II. Mathematical Model

### A. Definitions

Let $\boldsymbol{\xi}_{abc} = [\xi_a\ \xi_b\ \xi_c]^\top$ be any variable in the $abc$ reference frame. The Clarke transformation allows its representation in the $\alpha\beta$ reference frame, i.e., $\boldsymbol{\xi}_{\alpha\beta} = [\xi_\alpha\ \xi_\beta]^\top$, as follows:

$$\boldsymbol{\xi}_{\alpha\beta} = \boldsymbol{K}\boldsymbol{\xi}_{abc} \tag{1}$$

where $\boldsymbol{K}$ is the transformation matrix

$$\boldsymbol{K} = \frac{2}{3}\begin{bmatrix} 1 & -\frac{1}{2} & -\frac{1}{2} \\ 0 & \frac{\sqrt{3}}{2} & -\frac{\sqrt{3}}{2} \end{bmatrix}. \tag{2}$$

Based on this transformation, the three-phase instantaneous power $\boldsymbol{s}_{3\phi}$ can be expressed as

$$\boldsymbol{s}_{3\phi} = \begin{bmatrix} p_{3\phi} \\ q_{3\phi} \end{bmatrix} = \frac{3}{2}\begin{bmatrix} v_\alpha i_\alpha + v_\beta i_\beta \\ v_\alpha i_\beta - v_\beta i_\alpha \end{bmatrix}. \tag{3}$$

Lastly, the time-average value of an arbitrary periodic quantity $v(t)$ during a period $T$ is defined as

$$\langle v \rangle = \frac{1}{T}\int_0^T v(t)dt. \tag{4}$$

### B. Grid-Tied PV CHB Inverter Model

The grid-tied PV CHB inverter is shown in Fig. 1(a). Each inverter phase comprises an array of $N$ series-connected SMs so that the phase voltages correspond to $v_{abc} = \sum_{j=1,\dots,N} v_{abc}^j$, where $v_{abc}^j$ are the SM voltages. The grid voltages $\boldsymbol{v}_{g,abc} = [v_{ga}\ v_{gb}\ v_{gc}]^\top$ are assumed to be balanced with angular frequency $\omega = 2\pi f$, where $f$ is the rated grid frequency. The grid currents being injected by the inverter and the system common-mode voltage are given by $\boldsymbol{i}_{g,abc} = [i_{ga}\ i_{gb}\ i_{gc}]^\top$ and

$v_0$, respectively. Thus, the inverter is modeled by (5) and (6)

$$\sum_{j=1}^{N} v_k^j = L\frac{di_{gk}}{dt} + Ri_{gk} + v_{gk} + v_0, \quad k = a,\, b,\, c \tag{5}$$

$$0 = i_{ga} + i_{gb} + i_{gc}. \tag{6}$$

The SMs have two stages, i.e., multiple parallel-connected isolated dc–dc converters and three-level HB inverters, as shown in Fig. 1(b). The rated voltage for each SM dc-links $u_k^j$ is $V_{\text{dc}}$. In this work, an average model of the HB inverter has been utilized to implement the PS-MPC scheme. Accordingly, each SM is modeled using the voltages $v_k^j$ and modulation indexes $m_k^j$ as presented in the following equation:

$$v_k^j = u_k^j m_k^j. \tag{7}$$

Finally, as will be elucidated in Section III-D, $m_k^j$ is modulated by a phase-shifted pulsewidth modulation (PS-PWM) stage, which allows the inverter to reduce the switching frequency as many times as twice the number of SMs per phase. A fundamental part of this work is designing a common-mode signal with low-harmonic content to be added to the modulation indexes to extend the converter's operating zone regarding interphase power imbalances.

### C. Control Problem Formulation

This study aims to determine the OCMV to be modulated by the converter to transfer all the available power in the PV sources to the grid, considering balanced currents and minimal rms value for the CMV. For the problem at hand, the modulation frequency of the PS-PWM modulation stage is assumed to be high enough to analyze the problem in a continuous-time frame. Then, the harmonic content due to the inverter switching is not considered. Since filter losses are neglected, the active power injected into the grid $p_{i,3\phi}$ equals the active power available from the PV sources in all three phases, which can be stated as

$$p_{i,3\phi} = p_{ia} + p_{ib} + p_{ic}. \tag{8}$$

Thus, given the power factor angle $\varphi$, the current flowing from the converter to the grid can be calculated from (3) as follows:

$$\boldsymbol{i}_{g,\alpha\beta} = \begin{bmatrix} A & B \\ -B & A \end{bmatrix} \boldsymbol{v}_{g,\alpha\beta} \tag{9}$$

where $A = \frac{2}{3}\frac{p_{i,3\phi}}{|\boldsymbol{v}_g|^2}$, $B = \frac{2}{3}\frac{q_{i,3\phi}}{|\boldsymbol{v}_g|^2}$, and the reactive power $q_{i,3\phi}$ at the grid side is defined as

$$q_{i,3\phi} = p_{i,3\phi}\tan(\varphi). \tag{10}$$

Thereupon, if we multiply (5) by the line current $i_{gk}$ under the nonlosses filter assumption, and we temporarily average it, we obtain

$$\langle v_k i_{gk}\rangle = L\left\langle \frac{di_{gk}}{dt} i_{gk}\right\rangle + \langle v_{gk} i_{gk}\rangle + \langle v_0 i_{gk}\rangle, \quad k = a,\, b,\, c. \tag{11}$$

In (11), the first term is the available power in phase $k$, $p_{ik}$; the second term is zero because $i_{gk}$ is a harmonic function (assuming $v_g$ as a harmonic function); and the third term is the power injected into the grid by phase $k$, which is balanced and equal to $\frac{p_{i,3\phi}}{3}$. Using these definitions, (11) is simplified to

$$\Delta p_k = p_{ik} - \frac{p_{i,3\phi}}{3} = \langle v_0 i_{gk}\rangle, \quad k = a,\, b,\, c \tag{12}$$

where $\Delta p_k$ defines the asymmetry level of the available power in each converter phase.

Accordingly, the optimization problem for achieving minimal rms value for the common-mode voltage can be written as follows:

$$\min_{v_0} \ \langle v_0^2\rangle \tag{13a}$$

$$\text{s.t. (12)}$$

$$v_k^{\min} \le v_k^{\text{sym}} + v_0 \le v_k^{\max}, \quad k = a, b, c \tag{13b}$$

where $v_k^{\min}$ and $v_k^{\max}$ are the minimum and maximum inverter voltages in phase $k$, and $\boldsymbol{v}_{abc}^{\text{sym}} = [v_a^{\text{sym}}\ v_b^{\text{sym}}\ v_c^{\text{sym}}]^\top$ is the symmetrical component of the converter phase voltage vector, which can be obtained rewriting (5) using (1) as follows:

$$\boldsymbol{v}_{\alpha\beta}^{\text{sym}} = \begin{bmatrix} 1+\omega LB & -\omega LA \\ \omega LA & 1+\omega LB \end{bmatrix} \boldsymbol{v}_{g,\alpha\beta} \tag{14}$$

and then applying the inverse Clarke transform to (14) to get

$$\boldsymbol{v}_{abc}^{\text{sym}} = \frac{3}{2}\boldsymbol{K}^\top \boldsymbol{v}_{\alpha\beta}^{\text{sym}}. \tag{15}$$

A simplified version of the optimization model shown in (13) can be obtained if the bounds of the common-mode voltage are defined as

$$v_0^{\min} = \max_k \left\{v_k^{\min} - v_k^{\text{sym}}\right\} \tag{16}$$

$$v_0^{\max} = \min_k \left\{v_k^{\max} - v_k^{\text{sym}}\right\} \tag{17}$$

and the $\alpha\beta$ transformation (1) is used in (11) yielding

$$(\text{P}_0) \quad \min_{v_0} \ \langle v_0^2\rangle \tag{18a}$$

$$\text{s.t. } \Delta p_\alpha = \langle v_0 i_{g\alpha}\rangle \tag{18b}$$

$$\Delta p_\beta = \langle v_0 i_{g\beta}\rangle \tag{18c}$$

$$v_0^{\min} \le v_0 \le v_0^{\max} \tag{18d}$$

where the asymmetry level $\Delta\boldsymbol{p}_{\alpha\beta} = [\Delta p_\alpha\ \Delta p_\beta]^\top$ of the available power in the $\alpha\beta$ reference frame is calculated from $\Delta\boldsymbol{p}_{abc} = [\Delta p_a\ \Delta p_b\ \Delta p_c]^\top$ as follows:

$$\Delta\boldsymbol{p}_{\alpha\beta} = \boldsymbol{K}\Delta\boldsymbol{p}_{abc}. \tag{19}$$

In the formulation $(\text{P}_0)$, the decision variable is the common-mode voltage $v_0$ in a single period. As the objective function (18a) is proportional to the squared-rms value of $v_0$, it minimizes the harmonic distortion of $v_0$. Then, to maintain a balanced current flow from the converter to the grid as deduced in (12), the average value in a single period of the product between $v_0$ and each orthogonal component of the grid current $\boldsymbol{i}_{g,\alpha\beta}$ must match the power imbalance levels $\Delta\boldsymbol{p}_{\alpha\beta}$ according to constraints (18b) and (18c). Lastly, considering the theoretical voltage levels, the converter's feasibility of effectively materializing $v_0$ in all

phases depends on the voltage gaps between the available dc voltages ($v_k^{\min}$ and $v_k^{\max}$) and the symmetrical phase voltage $v_k^{\text{sym}}$ in each phase $k$. To guarantee the accomplishment of this condition, the constraint (18d) is included in the optimization model ($\mathrm{P}_0$).

The formulation ($\mathrm{P}_0$) corresponds to a constrained linear-quadratic control problem, which involves only a single decision variable. The optimal solution and its real-time implementation are presented in the following section.

## III. Solution Approach

### A. Control Problem Solution

To solve ($\mathrm{P}_0$), necessary and sufficient conditions can be obtained using the maximum principle of Pontryagin [15], [16]. A specific application of this principle to solve ($\mathrm{P}_0$) can be found in [17], from whose results it is possible to determine the analytical solution for the optimal value of common-mode voltage $v_0^\star$ as

$$v_0^\star = \text{mid}\{v_0^{\min},\ \boldsymbol{\psi}_{\alpha\beta}^\top \boldsymbol{i}_{g,\alpha\beta},\ v_0^{\max}\} \tag{20}$$

where $\boldsymbol{\psi}_{\alpha\beta} = [\psi_\alpha\ \psi_\beta]^\top$ is a vector of multipliers that permits $v_0^\star$ to satisfy the boundary conditions (18b) and (18c).

***1) Relaxed Case:*** When no bounds are included in the common-mode voltage, the optimal values for $\psi_\alpha$ and $\psi_\beta$ are directly obtained from the solution of the following linear equations system:

$$\Delta p_\alpha = \psi_\alpha \langle i_{g\alpha}^2 \rangle + \psi_\beta \langle i_{g\alpha} i_{g\beta} \rangle \tag{21}$$

$$\Delta p_\beta = \psi_\alpha \langle i_{g\alpha} i_{g\beta} \rangle + \psi_\beta \langle i_{g\beta}^2 \rangle. \tag{22}$$

Considering that $i_{g\alpha}$ and $i_{g\beta}$ are orthogonal harmonic functions, the values for $\psi_\alpha$ and $\psi_\beta$ are

$$\psi_k = \frac{2}{|\boldsymbol{i}_g|^2} \Delta p_k, \quad k = \alpha, \beta \tag{23}$$

and then the OCMV in the relaxed case is given by

$$v_{0,\,\text{relax.}}^\star = \Delta \boldsymbol{p}_{\alpha\beta}^\top \boldsymbol{K}_{pq}^{-1} \boldsymbol{v}_{g,\alpha\beta} \tag{24}$$

where the matrix $\boldsymbol{K}_{pq}$ is

$$\boldsymbol{K}_{pq} = \frac{1}{3} \begin{bmatrix} p_{i,3\phi} & -q_{i,3\phi} \\ q_{i,3\phi} & p_{i,3\phi} \end{bmatrix}. \tag{25}$$

Note that, from (24), the OCMV in the relaxed case is a fundamental-frequency harmonic function whose magnitude depends on the power imbalance level, the total available power, the power factor, and the grid voltage.

***2) Voltage-Bounded Case:*** When the voltage bounds are included, the solution of the optimal control problem ($\mathrm{P}_0$) can be determined by calculating the vector of multipliers $\boldsymbol{\psi}_{\alpha\beta}$ that satisfies constraints (18b) and (18c), i.e., the solution of the equations system

$$\Delta \boldsymbol{p}_{\alpha\beta} = \langle \text{mid}\{v_0^{\min},\ \boldsymbol{\psi}_{\alpha\beta}^\top \boldsymbol{i}_{g,\alpha\beta},\ v_0^{\max}\} \boldsymbol{i}_{g,\alpha\beta} \rangle. \tag{26}$$

Consequently, the OCMV can be achieved by solving (26) and evaluating $\boldsymbol{\psi}_{\alpha\beta}$ in (20). A remarkable feature is that $\boldsymbol{\psi}_{\alpha\beta}$ is not grid voltage angle dependent. It is because the accomplishment of constraints (18b) and (18c) by a common-mode voltage $v_0$, given a fixed power imbalance vector $\Delta \boldsymbol{p}_{\alpha\beta}$, is evaluated for an entire period $T$. Therefore, considering that the grid voltage magnitude, the power factor, and the available power in each phase change at a slower time rate than the current controllers, it is crucial to mention that $\boldsymbol{\psi}_{\alpha\beta}$ can be determined for a fixed time frame, but considering that their values can be applied following a rolling horizon optimization scheme.

### B. Feasible Domains

A zero-sequence injection method's feasible domain is where a common-mode voltage enables full power transfer despite asymmetrical power distribution among the phases, i.e., inter-phase power imbalance. For the sake of simplicity, the subsequent feasible domains are derived assuming that

$$v_k^{\max} = -v_k^{\min} = V_{\max}, \quad k = a,\ b,\ c \tag{27}$$

where $V_{\max}$ is a constant voltage.

For the relaxed case, i.e., where $v_{0,\,\text{relax.}}^\star$ is a fundamental-frequency harmonic function, the feasible domain $\mathcal{F}$ is directly obtained from (13b) and (24) as follows:

$$\begin{aligned} \mathcal{F} = \Bigg\{ \Delta \boldsymbol{p}_{\alpha\beta} \in \mathbb{R}^2 :\ & \\ r^2 \geq & \left( \frac{\Delta p_\alpha}{p_{i,3\phi}} + \frac{1}{3} \right)^2 + \left( \frac{\Delta p_\beta}{p_{i,3\phi}} - \frac{1}{3} \left( \tan(\varphi) + \rho \right) \right)^2 \\ r^2 \geq & \left( \frac{\Delta p_\alpha}{p_{i,3\phi}} - \frac{1}{6} \left( 1 - \sqrt{3} \left( \tan(\varphi) + \rho \right) \right) \right)^2 \\ & + \left( \frac{\Delta p_\beta}{p_{i,3\phi}} + \frac{1}{6} \left( \tan(\varphi) + \sqrt{3} + \rho \right) \right)^2 \\ r^2 \geq & \left( \frac{\Delta p_\alpha}{p_{i,3\phi}} - \frac{1}{6} \left( 1 + \sqrt{3} \left( \tan(\varphi) + \rho \right) \right) \right)^2 \\ & + \left( \frac{\Delta p_\beta}{p_{i,3\phi}} + \frac{1}{6} \left( \tan(\varphi) - \sqrt{3} + \rho \right) \right)^2 \Bigg\} \end{aligned} \tag{28}$$

where

$$r = \frac{V_{\max}}{3|\boldsymbol{v}_g| \cos(\varphi)}, \qquad \rho = \omega L A \sec^2(\varphi). \tag{29}$$

In Fig. 2, the feasible region $\mathcal{F}$ is shown for $\frac{p_{i,3\phi}}{3} = \frac{2}{3}$ p.u. and different power factors. Note that $\mathcal{F}$ is smaller as the power factor reduces because of the greater required symmetrical voltage in each phase.

On the other hand, the OCMV method feasible domain $\mathcal{O}$ is deduced from (13b) and (20). It corresponds to a quasi-circular region, as shown in Fig. 2. As the analytical form of $\mathcal{O}$ is complicated to be stated, we obtained the formula of the largest circular feasible domain $\bar{\mathcal{O}} \subset \mathcal{O}$ as follows:

$$\bar{\mathcal{O}} = \left\{ \Delta \boldsymbol{p}_{\alpha\beta} \in \mathbb{R}^2 :\ \frac{\|\Delta \boldsymbol{p}_{\alpha\beta}\|}{p_{i,3\phi}} \leq \frac{\sec(\varphi)}{3|\boldsymbol{v}_g|} \kappa_0 \right\} \tag{30}$$

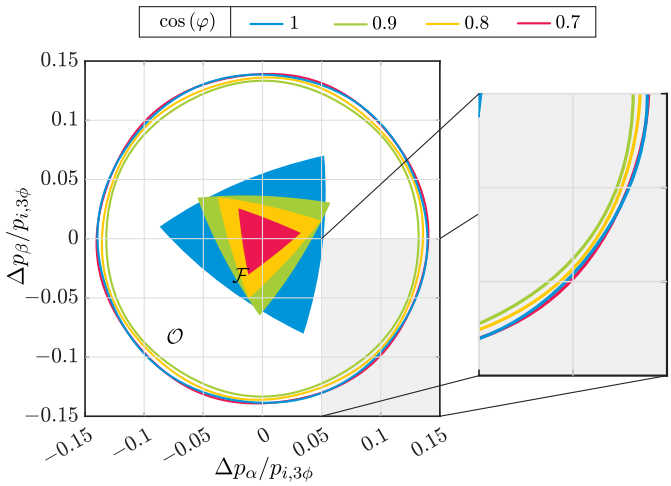


Fig. 2. Feasible domain $\mathcal{O}$ and feasible domains $\mathcal{F}$ for various power factors $\cos(\varphi)$ considering $\frac{p_{i,3\phi}}{3} = \frac{2}{3}$ p.u.

where $\|\cdot\|$ is the euclidean norm and

$$\kappa_0 = \frac{4}{\pi}V_{\max} - \left(\frac{3}{2\pi} + \frac{\sqrt{3}}{3}\right)|\boldsymbol{v}_g|\sqrt{(1+\omega LB)^2 + (\omega LA)^2}. \tag{31}$$

To summarize the operating region of a grid-tied CHB inverter, the points where the OCMV can handle interphase power imbalances while injecting balanced grid currents are included in $\mathcal{O}$. In particular, the points where the OCMV is a fundamental-frequency pure-sinusoidal function belong to $\mathcal{F}$. Consequently, the relation between the described feasible sets is $\mathcal{F} \subset \mathcal{O}$.

### C. Distributed Algorithm for the OCMV Implementation

In practice, calculating $\boldsymbol{\psi}_{\alpha\beta}$ in a real-time control platform can be carried out by expressing (26) as a root-finding problem. Subsequently, the problem can be solved numerically by employing the Newton–Raphson (NR) method. However, the execution of an NR method in real time is computationally demanding. Therefore, to avoid task overruns, we proposed a distributed numerical method that executes one iteration per sampling period $T_s$ of the current control scheme to iteratively calculate $\boldsymbol{\psi}_{\alpha\beta}$. The steps involved in this distributed algorithm are presented in the flowchart shown in Fig. 3.

First, we expressed (26) as follows:

$$\boldsymbol{F}_{\alpha\beta}\left(\boldsymbol{\psi}_{\alpha\beta}\right) = \langle \text{mid}\left\{v_0^{\min},\ \boldsymbol{\psi}_{\alpha\beta}^{\top}\boldsymbol{i}_{g,\alpha\beta},\ v_0^{\max}\right\}\boldsymbol{i}_{g,\alpha\beta}\rangle - \Delta\boldsymbol{p}_{\alpha\beta}. \tag{32}$$

Then, the zeros of the equation $\boldsymbol{F}_{\alpha\beta}(\boldsymbol{\psi}_{\alpha\beta}) = 0$ can be recursively determined by (33), i.e., the NR method

$$\boldsymbol{\psi}_{\alpha\beta}^{(\ell+1)} = \boldsymbol{\psi}_{\alpha\beta}^{(\ell)} - \boldsymbol{J}^{-1}\left(\boldsymbol{\psi}_{\alpha\beta}^{(\ell)}\right)\boldsymbol{F}_{\alpha\beta}\left(\boldsymbol{\psi}_{\alpha\beta}^{(\ell)}\right) \tag{33}$$

where $\boldsymbol{J}\left(\boldsymbol{\psi}_{\alpha\beta}^{(\ell)}\right) = \nabla\boldsymbol{F}_{\alpha\beta}\left(\boldsymbol{\psi}_{\alpha\beta}^{(\ell)}\right)$ is the Jacobian matrix of $\boldsymbol{F}_{\alpha\beta}$, whose components $J_{ij}$, with $i, j \in \{\alpha, \beta\}$, are calculated employing the centered difference formula as

$$J_{ij}\left(\boldsymbol{\psi}_{\alpha\beta}^{(\ell)}\right) = \frac{F_i\left(\boldsymbol{\psi}_{\alpha\beta}^{(\ell)} + h\boldsymbol{e}_j\right) - F_i\left(\boldsymbol{\psi}_{\alpha\beta}^{(\ell)} - h\boldsymbol{e}_j\right)}{2h} \tag{34}$$

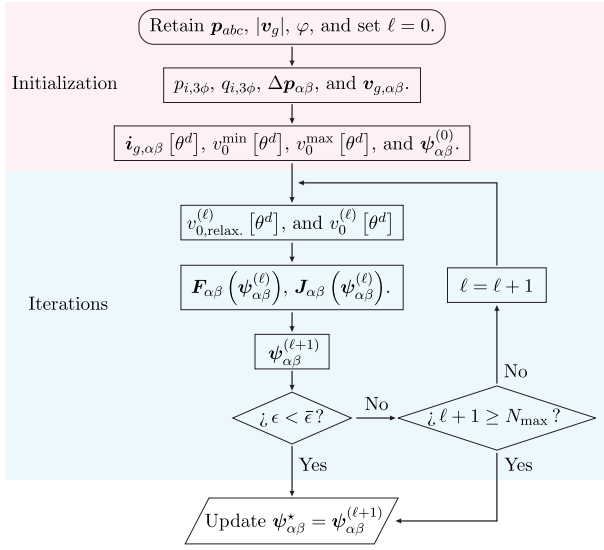


Fig. 3. Flowchart of the distributed algorithm for the OCMV's iterative calculation.

where $h > 0$ and $\boldsymbol{e}_j$ are the unit vectors in $\mathbb{R}^2$

$$\boldsymbol{e}_\alpha = [1\ 0]^\top, \qquad \boldsymbol{e}_\beta = [0\ 1]^\top. \tag{35}$$

At this point, it is important to mention that the variables employed to calculate $\boldsymbol{F}_{\alpha\beta}(\boldsymbol{\psi}_{\alpha\beta})$, in practical terms, correspond to sampled signals. These entities are $\boldsymbol{i}_{g,\alpha\beta}[\theta^d]$, $v_0^{\min}[\theta^d]$, and $v_0^{\max}[\theta^d]$, which are calculated and stored in the starting interruption where the inputs $\boldsymbol{p}_{abc} = [p_a\, p_b\, p_c]^\top$, $|\boldsymbol{v}_g|$, and $\varphi$ are retained until the algorithm updates its output $\boldsymbol{\psi}_{\alpha\beta}^{\star}$. This step is called *Initialization*, as shown in Fig. 3. Then, to determine these sampled variables, $\boldsymbol{v}_{g,\alpha\beta}$ is given by

$$\boldsymbol{v}_{g,\alpha\beta} = |\boldsymbol{v}_g|\,[1\,0]^\top. \tag{36}$$

Then, $p_{i,3\phi}$, $q_{i,3\phi}$, and $\Delta\boldsymbol{p}_{\alpha\beta}$ are calculated using (8), (10), and (19). Subsequently, the sampled grid current $\boldsymbol{i}_{g,\alpha\beta}[\theta^d]$ can be determined by calculating $\boldsymbol{i}_{g,\alpha\beta}$ from (9) and using the sampled interval $\theta^d$ conceived as

$$\theta^d = \left[0\ \ \frac{2\pi}{N^d-1}\ \ \cdots\ \ \left(N^d-2\right)\frac{2\pi}{N^d-1}\ \ 2\pi\right] \tag{37}$$

where $N^d$ is the number of samples. This way, $\boldsymbol{i}_{g,\alpha\beta}[\theta^d]$ is calculated as follows:

$$\boldsymbol{i}_{g,\alpha\beta}\left[\theta^d\right] = \begin{bmatrix} i_{g,\alpha}\cos\left(\theta^d\right) - i_{g,\beta}\sin\left(\theta^d\right) \\ i_{g,\alpha}\sin\left(\theta^d\right) + i_{g,\beta}\cos\left(\theta^d\right) \end{bmatrix}. \tag{38}$$

Afterwards, the sampled variables $v_0^{\min}[\theta^d]$ and $v_0^{\max}[\theta^d]$ can be calculated by determining $\boldsymbol{v}_{\alpha\beta}^{\text{sym}}$ from (14), then computing $\boldsymbol{v}_{\alpha\beta}^{\text{sym}}[\theta^d]$ as follows:

$$\boldsymbol{v}_{\alpha\beta}^{\text{sym}}\left[\theta^d\right] = \begin{bmatrix} v_\alpha^{\text{sym}}\cos\left(\theta^d\right) - v_\beta^{\text{sym}}\sin\left(\theta^d\right) \\ v_\alpha^{\text{sym}}\sin\left(\theta^d\right) + v_\beta^{\text{sym}}\cos\left(\theta^d\right) \end{bmatrix} \tag{39}$$

later evaluating $\boldsymbol{v}_{\alpha\beta}^{\text{sym}}[\theta^d]$ in (15) to get $\boldsymbol{v}_{abc}^{\text{sym}}[\theta^d]$, and finally using (16) and (17).

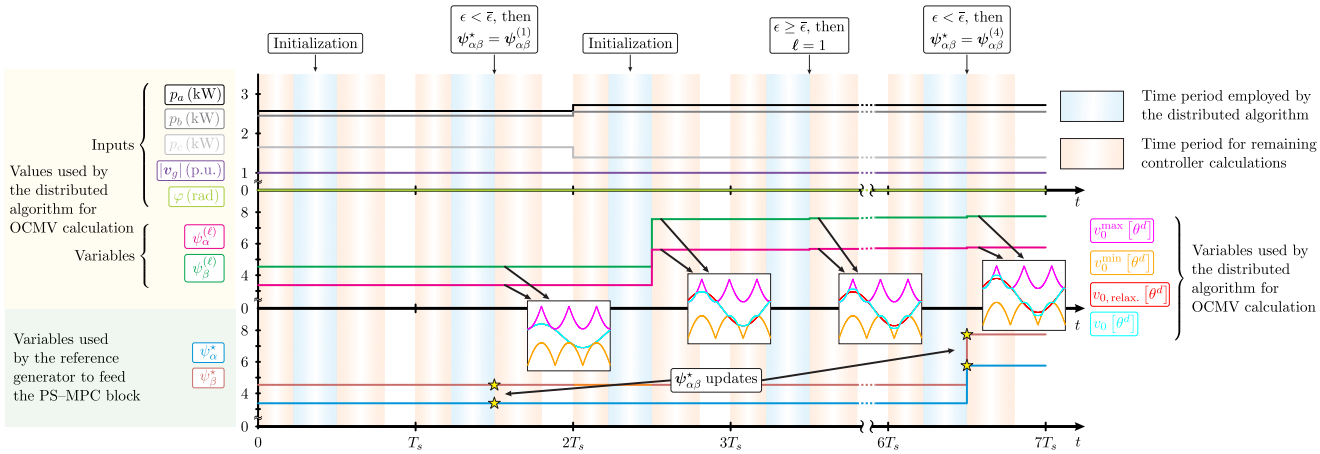


Fig. 4. Graphical representation of the working procedure employed by the distributed algorithm.

Lately, $\boldsymbol{\psi}^{(0)}_{\alpha\beta}$ is computed using (23) and the previously estimated values of $\Delta\boldsymbol{p}_{\alpha\beta}$ and $\boldsymbol{i}_{g,\alpha\beta}$. Once this step is completed, the algorithm waits until the next controller interruption to start the iterative process.

Subsequently, the step called *Iterations* begins by calculating the respective variables $v^{(\ell)}_{0,\text{relax.}}[\theta^d]$ and $v^{(\ell)}_{0}[\theta^d]$ by using

$$v^{(\ell)}_{0,\text{relax.}}\left[\theta^d\right] = \boldsymbol{\psi}^{(\ell)\top}_{\alpha\beta}\boldsymbol{i}_{g,\alpha\beta}\left[\theta^d\right] \tag{40}$$

and evaluating $v_0^{\min}[\theta^d]$, $v_0^{\max}[\theta^d]$, and $v^{(\ell)}_{0,\text{relax.}}[\theta^d]$ in (20).

Then, it is possible to compute both components of $\boldsymbol{F}_{\alpha\beta}(\boldsymbol{\psi}^{(\ell)}_{\alpha\beta})$ and the four terms $J_{ij}(\boldsymbol{\psi}^{(\ell)}_{\alpha\beta})$ by using the trapezoidal rule to evaluate the integrals in (32) and (34). Lately, Cramer's rule for $2 \times 2$ matrices is employed to directly compute $\boldsymbol{J}^{-1}(\boldsymbol{\psi}^{(\ell)}_{\alpha\beta})$, and finally $\boldsymbol{\psi}^{(\ell+1)}_{\alpha\beta}$ can be determined utilizing (33).

The Euclidean norm $\epsilon = \|\boldsymbol{\psi}^{(\ell+1)}_{\alpha\beta} - \boldsymbol{\psi}^{(\ell)}_{\alpha\beta}\|_2$ less than a pre-established value $\bar{\epsilon}$ is adopted as convergence criterion. Once the algorithm converges or reaches a given maximum number of iterations $N_{\max}$, $\boldsymbol{\psi}^{\star}_{\alpha\beta}$ is updated.

In addition, for the sake of understanding, a graphical representation showing two operating points is presented in Fig. 4. Initially, the system operates inside the feasible domain $\mathcal{F}$ so that the OCMV is equal to a pure-sinusoidal waveform, and then, the interphase power imbalance is increased leading the system to operate outside $\mathcal{F}$ but still inside $\mathcal{O}$, i.e., the OCMV must have harmonic components to deal with the power imbalance level. In the first case, the distributed algorithm can update $\boldsymbol{\psi}^{\star}_{\alpha\beta}$ between one and two current controller interruptions. In the second case, the distributed algorithm needs four iterations to converge. Therefore, the $\boldsymbol{\psi}^{\star}_{\alpha\beta}$ update takes place between four and five interruptions after the power imbalance change.

It is important to indicate that the distributed algorithm can be run within the controller calculations, so that, the updates related to $\boldsymbol{p}_{abc}$, $|\boldsymbol{v}_g|$, and $\varphi$ can be treated in the same interruption. Moreover, as the current controller starts after the distributed algorithm, the new $\boldsymbol{\psi}^{\star}_{\alpha\beta}$ value can be used in the same interruption.

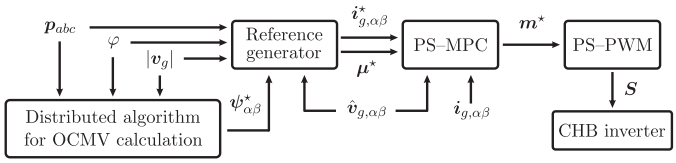


Fig. 5. Overall control scheme.

Finally, given the complexity of the control problem and its dependency on the system parameters, the distributed algorithm's parameters had to be set utilizing offline experimentation considering the real-time hardware limitations.

## D. Grid-Current Controller

Once the multipliers $\boldsymbol{\psi}^{\star}_{\alpha\beta}$ are determined, the reference variables to perform the grid-current control must be calculated. These operations are carried out by a reference generator whose goal is to compute both the reference grid currents $\boldsymbol{i}^{\star}_{g,\alpha\beta}$ and the reference modulation indexes $\boldsymbol{\mu}^{\star}$. First, $\boldsymbol{i}^{\star}_{g,\alpha\beta}$ is calculated evaluating $p_{i,3\phi}$, $\varphi$, and the estimated grid voltage $\hat{\boldsymbol{v}}_{g,\alpha\beta}$ given by the PLL in (9). Then, $\boldsymbol{\psi}^{\star}_{\alpha\beta}$, $\boldsymbol{i}^{\star}_{g,\alpha\beta}$, and $\hat{\boldsymbol{v}}_{g,\alpha\beta}$ are employed to get $v_0^{\star}$ using (20). Later, $\boldsymbol{\mu}^{\star}$ can be computed as follows:

$$\boldsymbol{\mu}^{\star} = \frac{\boldsymbol{v}^{\text{sym}}_{abc} + v_0^{\star}}{V_{dc}}. \tag{41}$$

In this way, the references are sent to the PS-MPC scheme block to control the grid currents.

The PS-MPC scheme presented in [18] was reformulated to control the symmetrical grid currents defined in (9). In this scheme, the modulation indexes of the SMs of each phase are updated sequentially so that the corresponding MPC problem is one step. In our application, the system state-space model was set up considering $\alpha\beta$ currents, grid voltages, and each SM's modulation index. The objective function comprised the $\alpha\beta$ currents quadratic error and the squared Euclidean distance between the optimal modulation indexes and $\boldsymbol{\mu}^{\star}$. It is crucial to mention that an active-set method was used to deal with optimal modulation indexes' real-time calculation.

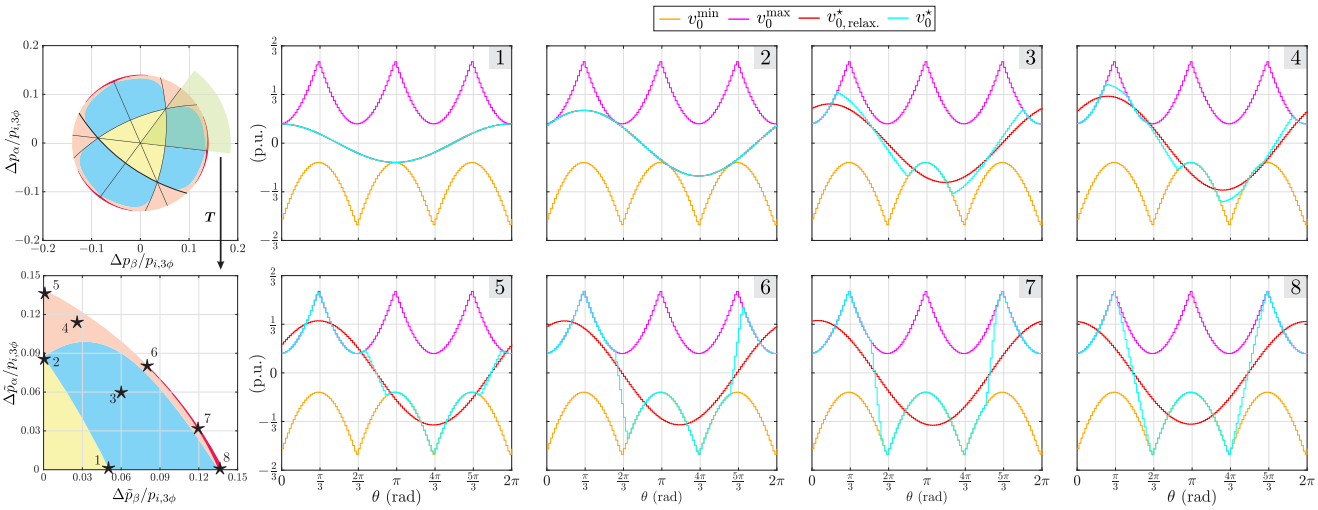


Fig. 6. First column: Feasible domain $\mathcal{O}$ (up) and transformed sextant with analyzed points (down). From the second to fifth column: Sampled waveform of the common-mode voltage max/min limits, relaxed solution, and the OCMV.

Finally, the overall control scheme is shown in Fig. 5 where the distributed algorithm, the reference generator, the PS-MPC scheme, and the PS-PWM block are represented.

## IV. Numerical Analysis

The following analysis aims to graphically show different representative operating points inside $\mathcal{O}$ for which the obtained OCMV waveform produces additional harmonics beyond the fundamental frequency. To analyze the OCMV and compare it with the prominent counterpart method, i.e., OZSI [11], a grid-tied seven-level CHB inverter has been used.

***1) OCMV Waveform:*** Depending on the interphase power imbalance level, the OCMV adopts a suitable fundamental and harmonic content to allow the grid-tied CHB inverter to inject balanced currents. First, the operating area is divided into six symmetrical radial sectors, i.e., sextants of $\mathcal{O}$, as shown in the first column of Fig. 6. Then, one of these sextants is transformed to be plotted in a quadrant of the $\Delta\tilde{\boldsymbol{p}}_{\alpha\beta}/p_{i,3\phi}$ plane. Finally, eight points were selected to visualize the OCMV in different cases called as $v_{0,(\star 1-8)}^{\star}$. The first two points, $\star 1$ and $\star 2$, have been placed on the border of $\mathcal{F}$. These points represent cases where $v_{0,\text{relax}}^{\star}$ are slightly in contact with the upper and lower bounds, i.e., $v_0^{\min}$ and $v_0^{\max}$. Therefore, the OCMV waveform in Fig. 6 is purely sinusoidal as shown in $v_{0,(\star 1)}^{\star}$ and $v_{0,(\star 2)}^{\star}$, respectively. Then, suppose the power imbalances increase and are represented by points $\star 3$ and $\star 4$. In these cases, $v_{0,(\star 3-4)}^{\star}$ includes harmonics with a fundamental-frequency component equal to the relaxed case $v_{0,\text{relax}}^{\star}$ to maintain a balanced current injection into the grid. Beyond that, and almost reaching $\partial\mathcal{O}$, points $\star 5$ to $\star 8$ represent severe interphase power imbalances, in which the OCMV waveform is highly distorted, but the required fundamental frequency component $v_{0,\text{relax}}^{\star}$ is successfully accomplished.

***1) Harmonic Content Comparison:*** This comparison aims to demonstrate that the proposed OCMV has superior performance against OZSI in terms of common-mode voltage harmonic content, which is essential to handle severe power imbalances effectively. Nevertheless, as will be elucidated, a minimal harmonic content exists, which translates into minimal THD, for dealing with severe power imbalances, as stated by the mathematical model $(\mathrm{P}_0)$. Consequently, a smooth transition from a fundamental frequency ZSV waveform to a distorted one is attained to dramatically reduce the harmonic content in the converter neutral terminal while keeping balanced grid currents. The THDs of the proposed OCMV and the OZSI are shown in Fig. 7. As expected, the THD is zero for both methods in $\mathcal{F}$. Beyond that, the OCMV smoothly increments its harmonic distortion to a maximum at $\partial\mathcal{O}$. On the contrary, the OZSI calculation concept leads to an abrupt jump at the border of $\mathcal{F}$. The additional harmonic content of OZSI produces almost 1.5 times higher distortion than OCMV until reaching $\partial\mathcal{O}$. In this feasible limit, both THDs are equal due to the uniqueness of the common-mode voltage at the maximum treatable power imbalances.

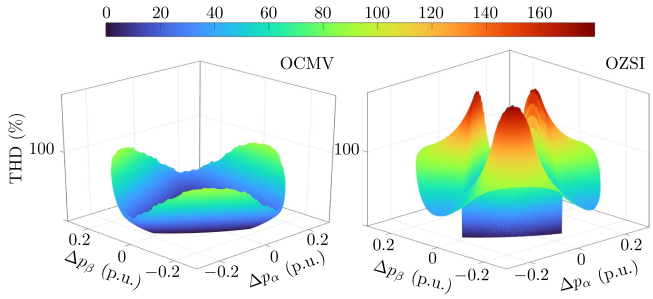


Fig. 7. THDs of the OCMV and the common-mode voltage proposed by [11] (OZSI).

To visualize the harmonic reduction improvements, the common-mode voltages for the OCMV and OZSI, and their FFTs are shown in Fig. 8 for power imbalance levels $\Delta\boldsymbol{p}_{\alpha\beta}$ equal to $(-0.08, -0.1)$, $(-0.15, -0.2)$, and $(-0.2, 0)$ p.u. extracted from Fig. 7.

In the upper row of Fig. 8, harmonic-distorted waveforms for the $v_{0,\text{OZSI}}$ can be seen, meanwhile, the proposed $v_0^{\star}$ clearly achieves less distorted waveforms for the same conditions. The

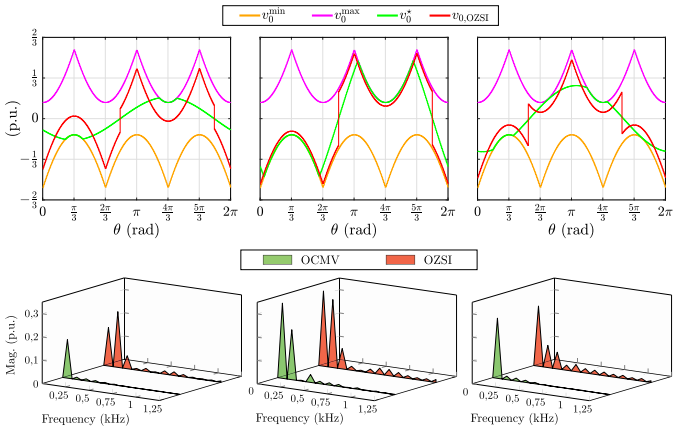


Fig. 8. Comparison of OCMV's and OZSI's waveforms and FFTs for $\Delta \boldsymbol{p}_{\alpha\beta}$ equal to $(-0.08, -0.1)$ (left), $(-0.15, -0.2)$ (center), and $(-0.2, 0)$ p.u. (right).

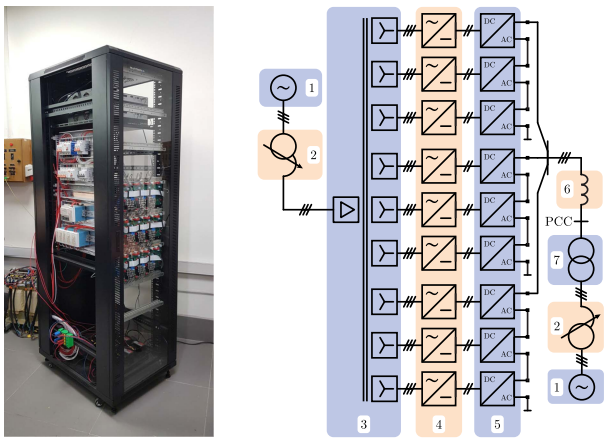


Fig. 9. Test bed and its unilinear diagram. Glossary: 1) Grid. 2) Variable autotransformer. 3) Multiwinding transformer. 4) Three-phase diode rectifiers. 5) HBs. 6) $L$ filter. 7) Isolation transformer.

TABLE I
EXPERIMENTAL SYSTEM PARAMETERS

| Parameter | Value | Parameter | Value |
|---|---|---|---|
| Rated power | 3 kVA | Grid frequency | 50 Hz |
| RMS grid voltage | $110\sqrt{3}$ V | Dc–links rated voltage | 70 V |
| Filter resistance | 0.2 Ω | Dc–links capacitance | 1 mF |
| Filter inductance | 8.3 mH | PSPWM carrier frequency | 1 kHz |

bottom row of Fig. 8 demonstrates that both waveforms exhibit identical fundamental-frequency voltages, thus dealing with the same interphase power imbalance level. However, the OCMV method always obtains less harmonic content as also shown for all the operating points in Fig. 7.

## V. EXPERIMENTAL VALIDATION

Once the highlighted features of the OCMV method were numerically analyzed, its experimental verification was carried out using the test bed presented in Fig. 9, whose parameters are shown in Table I. The proposed distributed algorithm was

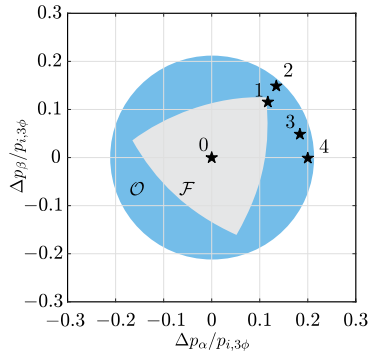


Fig. 10. Operating area with the experimental power imbalance cases.

designed so that 98% of the power imbalance cases within the feasible domain $\mathcal{O}$ converge using the following parameters $h = 10^{-4}$, $N^d = 360$, $\bar{\epsilon} = 10^{-6}$, and $N_{\max} = 8$. Specifically, the distributed algorithm execution takes 42.4 $\mu$s and 9.8 $\mu$s for the initialization and each iteration per interruption.

### A. Laboratory Setup

For the purpose of studying the real-time performance of the proposed OCMV, the laboratory setup intentionally excludes the PV panels and dc–dc converters. Actually, the OCMV is formulated to contribute at the grid side rather than manipulate the dc-side. Thus, each SM of the seven-level CHB converter was fed by a three-phase rectifier connected at each output winding of the multiwinding transformer. This configuration allowed us to extract a given power at each dc-link of the HBs. The point of common coupling (PCC) and the multiwinding transformer primary voltages were manually regulated using autotransformers. The laboratory grid voltage inherently contained fifth and seventh voltage harmonics. Therefore, sixth-harmonic oscillations in both active and reactive power were expected, considering the suitable performance of the current controller.

The proposed OCMV injection method and the current controller were implemented in an OPAL-RT OP4510 platform.

### B. Laboratory Experiments

This section aims to validate the OCMV implementation in a seven-level CHB inverter considering various power imbalance cases. The OCMV was calculated in real time for each case and added to the steady-state index modulations used as controller references.

***1) Steady-State Performance:*** Four power imbalance cases labeled 1 to 4 were imposed among converter phases while maintaining the desired active and reactive powers injected into the grid. The four cases are shown in the operating area drawing in Fig. 10. They were sequentially produced from the balanced condition 0 defined by $p_a = p_b = p_c = 1$ kW and unitary power factor. All the power imbalance cases have the same average active and reactive powers. The results of the experiments for each case, including the inverter voltages, the grid currents, the PCC voltages, and the active and reactive powers injected into the grid, are presented in Fig. 11.

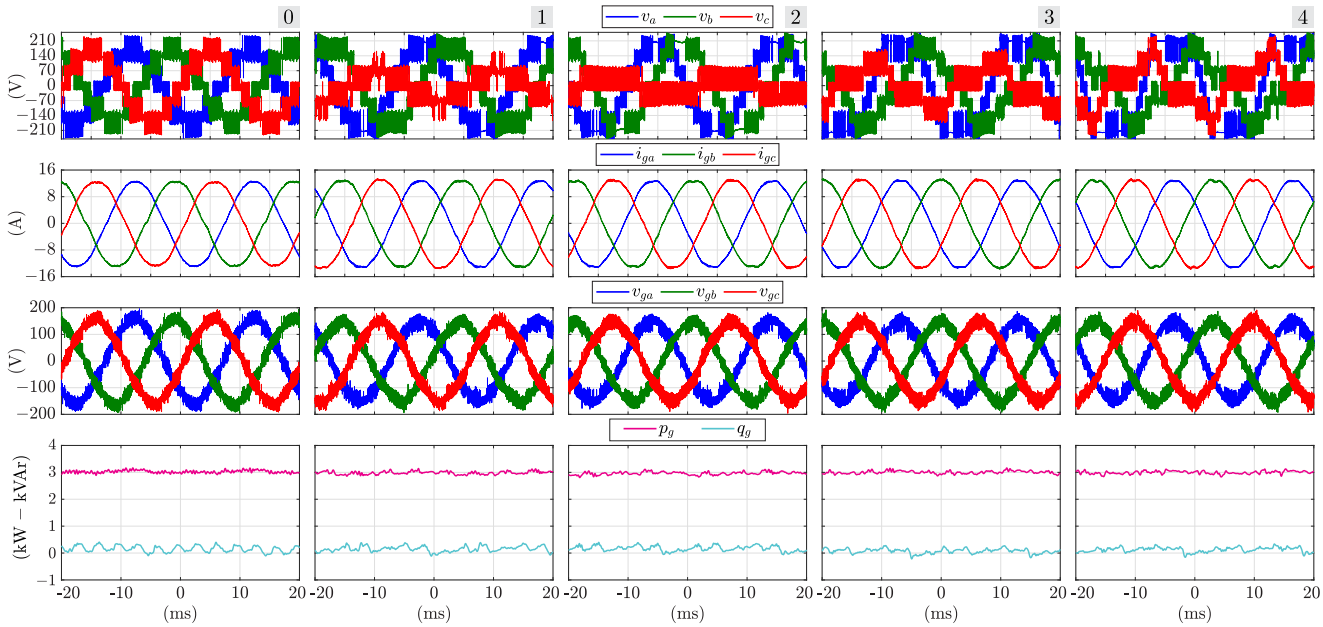


Fig. 11. Experimental results for each power imbalance case from 0 (first column) up to 4 (fifth column). Plots in each row: Inverter voltages (first row), grid currents (second row), PCC voltages (third row), and active/reactive powers injected into the grid (fourth row).

TABLE II
HARMONIC DISTORTION AND IMBALANCE LEVEL METRICS

| Case | | 0 | 1 | 2 | 3 | 4 |
|---|---|---|---|---|---|---|
| THDe (%) | $\boldsymbol{v}_{abc}$ | 5.5 | 5.8 | 8.4 | 19.2 | 30.0 |
| | $\boldsymbol{i}_{g,abc}$ | 2.8 | 2.6 | 2.7 | 2.1 | 2.4 |
| $\bar{i}_{g,1}$ (A) | | 12.87 | 13.25 | 13.20 | 13.33 | 13.27 |
| $\hat{\Delta} i_{g,1}$ (%) | | 0.4 | 1.0 | 1.0 | 0.8 | 1.0 |

From the first column of Fig. 11, i.e., the balanced operating condition, it was noted that the current controller could mitigate the PCC voltage harmonic content to keep balanced and low-distorted grid currents. The interaction between the fundamental frequency component of the grid current and the mentioned harmonic content at the PCC voltage originated sixth harmonics in the reactive power injected into the grid. Besides, the high-frequency harmonics due to the inverter voltage switching pattern induced high-order harmonics in the PCC voltage.

For the rest of the cases, the injected OCMV caused the SMs to operate saturated during some time intervals, as shown in the first row of Fig. 11. Nonetheless, the grid currents remained balanced and low distorted, and the active and reactive powers were maintained in their reference values, even considering severe power imbalances.

In particular, the equivalent THD (THDe) [19] was used to measure the harmonic content of the inverter voltages $\boldsymbol{v}_{abc}$ and the grid currents $\boldsymbol{i}_{g,abc}$. On the other hand, the fundamental-frequency amplitudes on the grid currents were calculated for each phase. Then, for each case, the grid current imbalance level $\hat{\Delta} i_{g,1}$ was determined as the maximum percentage deviation of the amplitudes regarding their mean value $\bar{i}_{g,1}$. The described metrics are presented in Table II. From Table II, it can

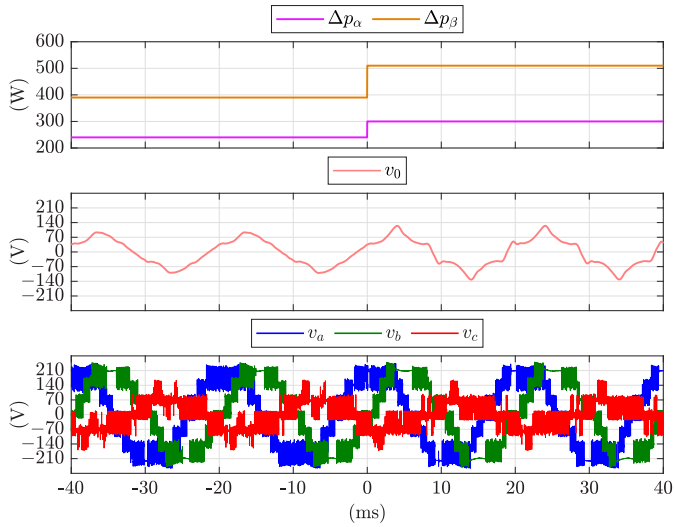


Fig. 12. Transient response to an interphase power imbalance change.

be highlighted that even though the voltage harmonic content increased until 30%, the grid current THDe was always in the permissible range, i.e., below 5%. Moreover, the imbalance level in the fundamental frequency of the grid currents was equal to or below 1% in all cases, verifying the OCMV injection method's effectiveness under severe interphase power imbalances in a grid-tied CHB inverter.

***2) Transient Performance:*** Finally, the proposed distributed algorithm for the OCMV implementation was tested for transient conditions. The inputs $\Delta \boldsymbol{p}_{\alpha\beta}$ are changed from $(240, 390)$ W to $(300, 510)$ W, as shown in Fig. 12. While such step change is physically unrealistic due to the slow MPPT

dynamic, examining the proposed OCMV's transient response is useful. Since $N_{\max}$ was set as 8, it is expected to update the value of $\psi^{\star}_{\alpha\beta}$ in less than $T_s N_{\max}$ seconds without delaying the calculation of $v_0^{\star}$. At this point, it is crucial to remark that every iteration is carried out at 6 kHz, i.e., one per current controller interruption. Moreover, as presented in Fig. 4, the real-time updating rate of the multipliers $\psi^{\star}_{\alpha\beta}$ given by the distributed algorithm corresponds to the delay between the change in either $\boldsymbol{p}_{abc}$, $\varphi$, or $|\boldsymbol{v}_g|$, and the adjustment of $v_0^{\star}$. In this case, the algorithm converged in 4 iterations, so the delay is 667 $\mu$s. This result means a negligible delay in the OCMV real-time calculation considering that the dynamic of the variables $\boldsymbol{p}_{abc}$, $\varphi$, and $|\boldsymbol{v}_g|$ are typically governed by slower secondary controllers, as opposed to the faster current controller of the converter.

## VI. Conclusion

This article formulated the interphase power imbalance problem for grid-tied CHB inverters as an optimal control problem. The optimal solution, OCMV, was derived, analyzed, and effectively implemented in an experimental setup. The proposed OCMV stands out due to its minimal harmonic content, which overcomes the additional distortion obtained with OZSI. The OCMV analytical form and its feasible domain were derived to illustrate the impact of the asymmetry level of the available interphase power on the voltage harmonic content. Furthermore, it was demonstrated that the OCMV can be easily implemented in a real-time control platform using the proposed time-distributed and iterative algorithm. An extensive simulation test was developed to appropriately adjust the algorithms to a wide range of imbalance operation conditions. Lastly, experimental results showed that implementing the OCMV allows the CHB to deal with severe power imbalances while keeping grid currents with a THDe lower than 2.8% and an imbalance level up to 1%.

## References


[1] IEA, "World energy outlook 2021," 2021. [Online]. Available: https://www.iea.org/reports/world-energy-outlook-2021

[2] REN21, "Renewables 2022 global status report," 2022. [Online]. Available: https://www.ren21.net/reports/global-status-report/

[3] D. Naghaviha, H. Nikkhajoei, and H. Karimi, *Step-By-Step Design of Large-Scale Photovoltaic Power Plants*. Hoboken, NJ, USA: Wiley, 2022.

[4] S. Kouro, B. Wu, H. Abu-Rub, and F. Blaabjerg, "Photovoltaic energy conversion systems," in *Power Electronics for Renewable Energy Systems, Transportation and Industrial Applications*. Hoboken, NJ, USA: Wiley, 2014, pp. 160–198.

[5] A. I. Elsanabary, G. Konstantinou, S. Mekhilef, C. D. Townsend, M. Seyedmahmoudian, and A. Stojcevski, "Medium voltage large-scale grid-connected photovoltaic systems using cascaded h-bridge and modular multilevel converters: A review," *IEEE Access*, vol. 8, pp. 223686–223699, 2020.

[6] X. Zhang, T. Zhao, W. Mao, D. Tan, and L. Chang, "Multilevel inverters for grid-connected photovoltaic applications: Examining emerging trends," *IEEE Power Electron. Mag.*, vol. 5, no. 4, pp. 32–41, Dec. 2018.

[7] *PVS800-57B Central Inverters: Hardware Manual*, Abb Solar Inverters, 2019.

[8] R. P. Aguilera, P. Acuna, C. A. Rojas, G. Konstantinou, and J. Pou, "Instantaneous zero sequence voltage for grid energy balancing under unbalanced power generation," in *Proc. IEEE Energy Convers. Congr. Expo.*, 2019, pp. 2572–2577.

[9] I. Marzo, A. Sanchez-Ruiz, J. A. Barrena, G. Abad, and I. Muguruza, "Power balancing in cascaded h-bridge and modular multilevel converters under unbalanced operation: A review," *IEEE Access*, vol. 9, pp. 110525–110543, 2021.

[10] Y. Yu, G. Konstantinou, B. Hredzak, and V. G. Agelidis, "Power balance of cascaded H-bridge multilevel converters for large-scale photovoltaic integration," *IEEE Trans. Power Electron.*, vol. 31, no. 1, pp. 292–303, Jan. 2016.

[11] Y. Yu, G. Konstantinou, B. Hredzak, and V. G. Agelidis, "Power balance optimization of cascaded H-bridge multilevel converters for large-scale photovoltaic integration," *IEEE Trans. Power Electron.*, vol. 31, no. 2, pp. 1108–1120, Feb. 2016.

[12] P. Sochor and H. Akagi, "Theoretical comparison in energy-balancing capability between star-and delta-configured modular multilevel cascade inverters for utility-scale photovoltaic systems," *IEEE Trans. Power Electron.*, vol. 31, no. 3, pp. 1980–1992, Mar. 2016.

[13] R. Sharma and A. Das, "Enhanced active power balancing capability of grid-connected solar PV fed cascaded h-bridge converter," *IEEE Trans. Emerg. Sel. Topics Power Electron.*, vol. 7, no. 4, pp. 2281–2291, Dec. 2019.

[14] F. Calderón, A. Angulo, and P. Acuna, "Optimal common-mode voltage for maximum power transfer of grid-tied PV CHB inverters," in *Proc. IEEE IECON 47th Annu. Conf. Ind. Electron. Soc.*, 2021, pp. 1–6.

[15] A. D. Lewis, "The maximum principle of pontryagin in control and in optimal control," in *Handouts for the Course Taught at the Universitat Politecnica de Catalunya*, CiteSeer, 2006.

[16] F. L. Lewis, D. Vrabie, and V. L. Syrmos, *Optimal Control*. Hoboken, NJ, USA: Wiley, 2012.

[17] R. Burachik, C. Kaya, and S. Majeed, "A duality approach for solving control-constrained linear-quadratic optimal control problems," *SIAM J. Control Optim.*, vol. 52, pp. 1423–1456, 2014.

[18] R. Cuzmar, J. Pereda, and R. P. Aguilera, "Phase-shifted model predictive control to achieve power balance of CHB converters for large-scale photovoltaic integration," *IEEE Trans. Ind. Electron.*, vol. 68, no. 10, pp. 9619–9629, Oct. 2021.

[19] *IEEE Standard Definitions for the Measurement of Electric Power Quantities Under Sinusoidal, Nonsinusoidal, Balanced, or Unbalanced Conditions*, Standard IEEE 1459-2010, 2010, doi: 10.1109/IEEESTD.2010.5439063.


**Felipe Calderón Rivera** (Student Member, IEEE) was born in Quilpué, Chile. He received the B.Sc. and M.Sc. degrees in electrical engineering from the Universidad Técnica Federico Santa María, Valparaíso, Chile, in 2017 and 2022, respectively. He is currently working toward the Ph.D. degree in electrical engineering with the DCE&S Research Group, Delft University of Technology, Delft, The Netherlands.

His research interests include optimal control strategies, multilevel converters, and EV charging systems.

**Alejandro Angulo** (Member, IEEE) was born in Osorno, Chile. He received the B.Sc. and M.Sc. degrees in electrical engineering from the Universidad Técnica Federico Santa María (UTFSM), Valparaíso, Chile, in 2004 and 2007, respectively, and the Ph.D. degree in operational research from Universidad de Chile, Santiago, Chile, in 2015.

He is currently an Assistant Professor with the Department of Electrical Engineering, UTFSM. His main research interests include integer programming, optimization applied to power converters control, model predictive control, optimization algorithms for embedded systems, and large-scale optimization applied to power system operation and planning.

**Pablo Acuna** (Member, IEEE) received the B.Sc. degree in electronics engineering, the B.Eng. degree in electronics engineering, and the Ph.D. degree in electrical engineering from the University of Concepción, Concepción, Chile, in 2004, 2007, and 2013, respectively.

From 2014 to 2017, he was a Research Associate with UNSW Sydney, Sydney, NSW, Australia. From 2018 to 2019, he was a Lecturer with RMIT University, Melbourne, VIC, Australia. He is currently an Associate Professor with the Universidad de Talca, Talca, Chile. His research interests include high-power conversion systems and their applications in industry, transportation, and utility.

**Andrés Mora** (Member, IEEE) received the B.Sc. and M.Sc. degrees with highest honors in electrical engineering from the Universidad Técnica Federico Santa María (UTFSM), Valparaíso, Chile, in 2010 and the Ph.D. degree in electrical engineering from the Universidad de Chile, Santiago, Chile, in 2019.

In 2011, he joined the Electrical Department, UTFSM, where he is currently an Associate Professor. Since 2023, he has been an Associate Researcher with the Advanced Center for Electrical and Electronic Engineering (AC3E), Valparaiso, Chile. His main research interests include advanced control techniques applied to modular multilevel converters, variable speed drives, and microgrids.

Dr. Mora was the recipient of IEEE TRANSACTIONS ON INDUSTRIAL ELECTRONICS Best Paper Award in 2019.